

**Understanding migratory flow caused by helicoid wire spacers in rod bundles
An experimental and theoretical study**

Bertocchi, F.; Rohde, M.; Kloosterman, J. L.

DOI

[10.1016/j.ijheatfluidflow.2019.108491](https://doi.org/10.1016/j.ijheatfluidflow.2019.108491)

Publication date

2019

Document Version

Final published version

Published in

International Journal of Heat and Fluid Flow

Citation (APA)

Bertocchi, F., Rohde, M., & Kloosterman, J. L. (2019). Understanding migratory flow caused by helicoid wire spacers in rod bundles: An experimental and theoretical study. *International Journal of Heat and Fluid Flow*, 80, Article 108491. <https://doi.org/10.1016/j.ijheatfluidflow.2019.108491>

Important note

To cite this publication, please use the final published version (if applicable).
Please check the document version above.

Copyright

Other than for strictly personal use, it is not permitted to download, forward or distribute the text or part of it, without the consent of the author(s) and/or copyright holder(s), unless the work is under an open content license such as Creative Commons.

Takedown policy

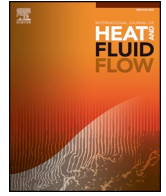
Please contact us and provide details if you believe this document breaches copyrights.
We will remove access to the work immediately and investigate your claim.

Green Open Access added to TU Delft Institutional Repository

'You share, we take care!' – Taverne project

<https://www.openaccess.nl/en/you-share-we-take-care>

Otherwise as indicated in the copyright section: the publisher is the copyright holder of this work and the author uses the Dutch legislation to make this work public.



Understanding migratory flow caused by helicoid wire spacers in rod bundles: An experimental and theoretical study

F. Bertocchi*, M. Rohde, J.L. Kloosterman

Faculty of Applied Sciences, Department of Radiation Science and Technology, Delft University of Technology, Mekelweg 15, Delft, 2629 JB, Netherlands

ARTICLE INFO

Keywords:

Rod bundle
Wire-wrap
Particle image velocimetry
Euler equation

ABSTRACT

The core of a Liquid Metal Fast Breeder Reactor (LMFBR) consists of cylindrical fuel rods that are wrapped by a helicoidally-wound wire spacer to enhance mixing and to prevent damage by fretting. It is known that the liquid metal close to the rod is forced to follow the wires, and that liquid metal further away from the rod crosses the wires (called: migratory flow). This work aims at gaining more insight into the physics behind migratory flow and to provide a model for its bending angle. To this purpose, the flow field in a 7-rods, wire-wrapped, hexagonal bundle with water is studied within the Reynolds number range of 4990–16330 by using Particle Image Velocimetry (PIV). Refraction of the light is minimized by using Fluorinated Ethylene Propylene (FEP), which is a refractive index-matching (RIM) material. These measurements confirm that liquid near the rod follows the helicoid path and bends cross-wise with respect to the wire further away from the rod. A theoretical model for the bending angle of the flow is derived from the Euler equations and shows that the bending is primarily caused by the pressure gradient field induced by the wire. The model shows a very good correspondence with the experimentally obtained PIV data. These findings improve our understanding of the physics at play in rod bundle flows with wrapped wires and can be of assistance in developing practical correlations for frictional pressure losses and heat transfer in such bundles.

1. Introduction

Rod bundles characterise the geometry of many industrial components, such as heat exchangers and the core of light water and liquid metal cooled nuclear reactors. In particular, the core of a Liquid Metal Fast Breeder Reactor (LMFBR) consists of a hexagonal bundle of rods, each wrapped by a wire wound helicoidally. These wires prevent damage by fretting of the fuel rod's cladding, and guide the liquid metal coolant close to the rods through the gaps between the pins enhancing radial heat transfer and, thus, improving the safe operation of the reactor. Over the years, considerable efforts have been dedicated to investigating wire-wrapped rod bundles; a comprehensive review of both experiments and numerical studies was provided in Moorthi et al. (2018). Sato et al. (2009) focused on the flow field inside the gap of a 7-rods, wire-wrapped hexagonal bundle, observing a lateral flow following the wrapping direction of the wire. Recently, the university of Texas performed a number of experiments in a 61-rods test section for code validation, as reported in Goth et al. (2018), and for studying vortical structures that may occur in the flow, as described in Nguyen and Hassan (2017) and in Nguyen et al. (2017). Computational Fluid Dynamics (CFD) studies have focused on modelling the flow around a

single wrapped-wire pin (Shams et al., 2018; Fischer et al., 2007), and on simulating the entire bundle for validation purposes (Pointer et al., 2008; Merzari et al., 2016; Obabko et al., 2016; Brockmeyer et al., 2017). Depending on the position of the wire, the flow is found, unexpectedly, to bend against the direction of the wire. This was called “migratory flow” in Ohtake et al. (1976), and ascribed to the increased hydraulic resistance caused by the wire inside the considered sub-channel. A physical model that is able to predict such a flow bending, however, was not provided, nor it is nowadays available

This work aims at measuring migratory flow, and to develop a model that explains and quantifies the bending of the flow. For this purpose, a 7-rods, wire-wrapped, hexagonal bundle has been designed and built to perform planar Particle Image Velocimetry (PIV) measurements of the flow in front of the wire around the central rod. Optical access, required for performing PIV measurements, has been achieved by partially replacing the metal of the rods with a refractive index-matching (RIM) material, being Fluorinated Ethylene Propylene (FEP), as described in Dominguez-Ontiveros and Hassan (2009), Mahmood (2011), Hosokawa et al. (2012) and in Bertocchi et al. (2018). This solution keeps the light refraction to a minimum, allowing for optical measurements inside the bundle.

* Corresponding author.

E-mail address: f.bertocchi@tudelft.nl (F. Bertocchi).

Nomenclature			
A	Bundle's total flow area (m ²)	\vec{r}	Vector position (m)
D_h	Bundle's hydraulic diameter (mm)	T	Fluid temperature (°C)
D	Rod diameter (mm)	t	Time (s)
D_w	Wire diameter (mm)	Δt	Time separation between two consecutive images (s)
\hat{e}_n, \hat{e}_s	Unit vectors perpendicular and tangent to the streamline	t_{FEP}	FEP wall thickness (mm)
$f_{\#}$	Lens aperture	\vec{U}	Velocity vector tangent to the streamline (ms ⁻¹)
h	Wire pitch (mm)	u, v	Vertical and transversal velocity components (ms ⁻¹)
i, j, τ	Indices	V_b	Bulk velocity based on the bundle's total flow area (ms ⁻¹)
L_d	Development length (m)	W/D	Closest wall distance-to-rod diameter ratio
M_o	Magnification factor	x, y, z	Transversal, vertical and out-of-plane directions
N	Number of recorded PIV images	\tilde{x}	Direction perpendicular to the wire
N_s	Number of sampled points along a streamline	$\Delta x, \Delta y$	Transversal and vertical pitch of the velocity vectors (mm)
n, s	Perpendicular and tangent directions in the streamlines' reference system	δz	Laser sheet thickness (out-of-plane) (mm)
P_h	Total wetted perimeter (mm)	α	Half-angle of the flow distributor (°)
P/D	Pitch to rod diameter ratio	β	Bending angle of the streamline (°)
p	Pressure (Pa)	γ	Wire's pitch angle (°)
Q	Volumetric flow rate (m ³ s ⁻¹)	θ	Wire angle with the horizontal (°)
R	Streamline's radius of curvature (m)	λ	Laser light wavelength (nm)
		ν	Kinematic viscosity (m ² s ⁻¹)
		ρ	Density (kg m ⁻³)

The approach is as follows:

1. The flow field at the front of the central wrapping wire is studied with PIV for six Reynolds numbers within the range of 4990 – 16330, at room temperature, and with water as working fluid.
2. The pressure gradient field close to the wire is retrieved from the measured velocity field and the discretised, two-dimensional Navier–Stokes equations.
3. A model, derived from the Euler equations, is derived for estimating both the pressure gradient normal to the wire and the bending angle of the flow streamlines.
4. The pressure gradient field obtained from the model is compared with the experimentally obtained field.
5. Finally, the theoretically predicted bending angle of the flow is compared with the experimental values to confirm the validity of the proposed model.

2. Experimental setup

The experimental apparatus consists of a water loop with a 7-rods hexagonal bundle having a spacing helical wire wrapped around each rod. The pitch-to-rod diameter ratio (P/D) is 1.11 and it is also equal to the nearest wall distance ratio-to-rod diameter (W/D). An hexagonal encasing of transparent polymethyl methacrylate (PMMA), commonly referred to as Perspex, encloses the bundle. The water flows top-down by gravity from an upper vessel through the bundle and is collected in a lower tank; a centrifugal pump provides the required head to circulate the water towards the upper vessel and to keep the water level in the vessel constant. A small in-house heat exchanger keeps the water temperature constant during the measurements, and the temperature is monitored with a thermocouple (Labfacility) installed inside the upper vessel. A valve with a linear response regulates the flow rate, which is monitored by both a magnetic (ABB - type HA3) and an ultrasonic flow meter (model TTFM100-B-HH-NG, B. M. Tecn. Industriali) independently.

2.1. Bundle geometry

The bundle consists of 7 rods arranged in a hexagonal lattice with a P/D of 1.11. A stainless steel wire is wound and point-welded around each rod. The main parameters of the hexagonal lattice and of the test section are listed in Table 1.

The sketch of the hexagonal test section casing is provided in Fig. 1.

The flow enters from the top and the water is distributed over the subchannels via a funnel-shaped flow distributor (Fig. 1c); after a development length of 1.5 m, the flow reaches the location of the measurements. The development length to reach fully turbulent conditions is based on CFD evidence (De Ridder et al., 2016). The internal structure of the flow distributor disrupts the large eddies that may develop in the stream, and it redistributes the flow uniformly among the subchannels of the bundle. Flow detachment from the walls of the distributor is avoided by adopting a divergent angle of 4°, as suggested in Idel'chik (1966). The divergent shape of the flow distributor may lead to entrapment of air bubbles in the flow. These would disturb the optical measurements to be performed in the rod bundle. However, the entrapment of air is observed below a flow rate of 9.00×10^{-4} m³s⁻¹, therefore the measured flow rates are kept above this threshold. Optical access around the central rod is ensured by partially replacing the stainless steel of the two front rods with heat-shrunk FEP (see Fig. 1b and 2 for further details), which has nearly the same refractive index of water. This minimises the refraction of light (Mahmood, 2011; Nguyen and Hassan, 2017; Bertocchi et al., 2018).

2.2. PIV System

2.2.1. Laser and seeding particles

The laser is a class-IV, diode pumped, 5 W laser with the wavelength $\lambda = 532$ nm (LaVision, Germany). The DaVis software allows for adjusting the separation time between the two laser pulses. The combination of a spherical and a cylindrical lens creates the laser sheet, which has a beam waist (the thinnest region of the sheet) thickness of 1 mm.

Table 1

Bundle's main dimensions. (see Nomenclature for a list of symbols) .

Parameter	Value	dim.
D	30	mm
D_w	3	mm
P/D	1.11	
W/D	1.11	
h	400	mm
θ	77	°
α	4	°
L_d	1.5	m
t_{FEP}	0.25	mm

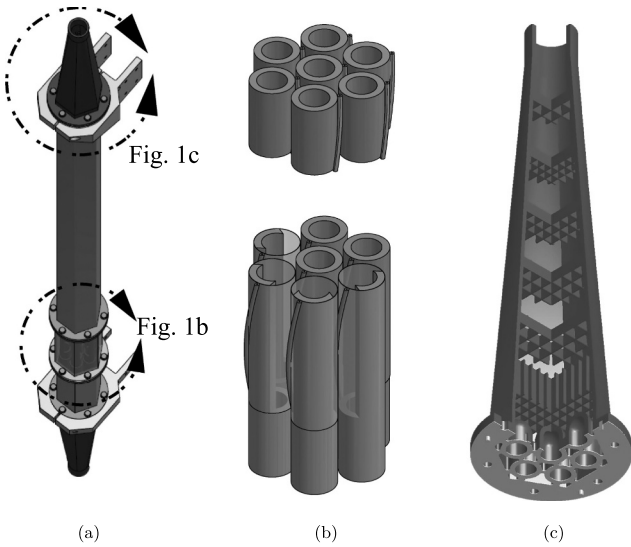


Fig. 1. a) An outer hexagonal casing, containing the rod bundle, is clamped to the supports. The PIV measurements are performed at the location of the transparent Perspex casing. b) Measurement section of the bundle where part of the rods is masked-out to make it more visible. FEP replaces part of the outer rods to provide decrease refraction of light. c) The inlet flow distributor conveys the fluid in the subchannels of the bundle; its internal structure breaks large vortices developed in the fluid falling from the top vessel.

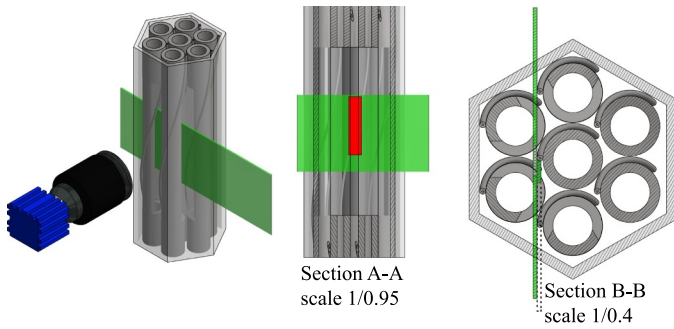


Fig. 2. Overview of the rod bundle test section as the laser light of the PIV system goes through: the area of interest (AOI) is the red rectangular area of the laser sheet. Front section (section A-A) and (top view (section B-B) of the bundle where the light sheet goes through the FEP in front of the central rod's wire. Section B-B shows the positions of the laser sheet corresponding to the preliminary measurement (dashed line), and to the measurement campaign focusing on the flow area in front of the wire. (For interpretation of the references to colour in this figure legend, the reader is referred to the web version of this article.)

The flow is seeded with borosilicate glass hollow spheres (LaVision, Germany) with an average density of 1.1 g m^{-3} and diameter falling within the range $9 - 13 \text{ }\mu\text{m}$.

2.2.2. Camera

The camera used for PIV measurements is a Complementary Metal-Oxide Semiconductor (CMOS) Imager MX-4M (LaVision, Germany) with 4 MP of resolution ($5.5 \text{ }\mu\text{m}$ of pixel size). The camera mounts a AF-S 50 mm F/1.4 (Nikon) lens with a magnification factor $M_0 = 0.13$. The depth of focus δz is given in Tropea et al. (2007) as

$$\delta z = 4 \left(1 + \frac{1}{M_0} \right)^2 f_{\#}^2 \lambda = 0.6 \text{ mm}, \quad (1)$$

where $f_{\#}$ is the lens aperture, and λ is the laser wavelength. An intensity correction algorithm consisting of a background subtraction is used to diminish the reflection from the internal components of the bundle.

2.2.3. PIV Vector calculation parameters

The calculation of the velocity fields is done in the PIV DaVis software as follows.

The recorded images are pre-processed with a sliding background subtraction algorithm available in the software. This method averages the local intensity of light around each particle. The mean value is then subtracted from the intensity value of each pixel to improve the local contrast. This method keeps intensity fluctuations at a minimum.

The velocity vectors are calculated by cross-correlating two consecutive images to detect the displacement of each particle. The cross-correlation is calculated over a so-called interrogation window whose size can be adjusted in the DaVis software. The multi-pass option allows for computing a first displacement field with an initial size of the interrogation window of 64×64 pixels. The interrogation window size is then decreased to 48×48 pixels during a second calculation.

The post-processing of the vector fields consists of a median filter to remove outliers, as in Westerweel (1994) and Nguyen et al. (2017). The resulting blank points are filled up with a vector interpolation algorithm available in the DaVis software.

2.3. Determining the pressure gradient field from the 2D Navier–Stokes equations

The pressure gradient normal to the wire, which is later needed to describe the migratory flow, is evaluated by means of the Navier–Stokes equations applied to the measured velocity fields. The laser sheet is positioned very close to the wire (i.e. tangent to it), therefore the out-of-plane velocity component is locally assumed to be negligible compared to the other two. Based on the experiments described in Nguyen et al. (2018), the out-of-plane velocity component is estimated to be equal at most to $10\%V_b$, for a Reynolds of 6300. Moreover, a recent numerical work (Song et al., 2019) showed that the local flow behaviour near the wire is independent of the Reynolds number. It is thus reasonable to assume that the relative magnitude of the out-of-plane velocity component near the wire does not strongly depend on the flow rate.

The Navier–Stokes equations are discretised in space and time following the approach described in de Kat and van Oudheusden (2010, 2011). The pressure gradient is expressed as follows:

$$\nabla p = -\rho \left[\frac{\partial \vec{U}}{\partial t} + (\vec{U} \cdot \nabla) \vec{U} - \nu \nabla^2 \vec{U} \right], \quad (2)$$

where \vec{U} is the velocity vector with components $(u; v; w)$. Assuming a two-dimensional flow, Eq. 2 is decomposed along x:

$$\begin{aligned} \frac{\partial p(x, y, t)}{\partial x} &= -\rho \left[\frac{\partial u(x, y, t)}{\partial t} + u(x, y, t) \frac{\partial u(x, y, t)}{\partial x} + v(x, y, t) \frac{\partial u(x, y, t)}{\partial y} - \nu \left(\frac{\partial^2 u}{\partial x^2} + \frac{\partial^2 u}{\partial y^2} \right) \right] \end{aligned} \quad (3)$$

and along y:

$$\begin{aligned} \frac{\partial p(x, y, t)}{\partial y} &= -\rho \left[\frac{\partial v(x, y, t)}{\partial t} + u(x, y, t) \frac{\partial v(x, y, t)}{\partial x} + v(x, y, t) \frac{\partial v(x, y, t)}{\partial y} - \nu \left(\frac{\partial^2 v}{\partial x^2} + \frac{\partial^2 v}{\partial y^2} \right) \right]. \end{aligned} \quad (4)$$

The time derivative term is discretised with a central finite difference scheme following (de Kat and van Oudheusden, 2011) considering a separation time between two consecutive images of 0.055 s. The same discretization scheme is used for the space derivatives. This leads, for the x direction, to

$$\frac{\partial p(i, j, \tau)}{\partial x} = -\rho \left[\frac{u(i, j, \tau + 1) - u(i, j, \tau - 1)}{2\Delta t} + u(i, j, \tau) \frac{u(i + 1, j, \tau) - u(i - 1, j, \tau)}{2\Delta x} + v(i, j, \tau) \frac{u(i, j + 1, \tau) - u(i, j - 1, \tau)}{2\Delta y} + v \left(\frac{u(i + 1, j, \tau) - 2u(i, j, \tau) + u(i - 1, j, \tau)}{(\Delta x)^2} + \frac{u(i, j + 1, \tau) - 2u(i, j, \tau) + u(i, j - 1, \tau)}{(\Delta y)^2} \right) \right] \quad (5)$$

and, similarly, for the y direction with y and v instead of x and u , respectively. Eq. 5 and the corresponding one for the y direction are averaged over the total recorded images to obtain the time-averaged pressure gradient components along x and y :

$$\frac{\partial p(i, j)}{\partial x} = \frac{1}{N} \sum_{\tau=1}^N \frac{\partial p(i, j, \tau)}{\partial x}, \quad (6)$$

and

$$\frac{\partial p(i, j)}{\partial y} = \frac{1}{N} \sum_{\tau=1}^N \frac{\partial p(i, j, \tau)}{\partial y}, \quad (7)$$

where N is the number of recorded PIV images. Finally, the time-averaged pressure gradient normal to the wire is estimated as

$$\frac{\partial p(i, j)}{\partial \bar{x}} = \frac{\partial p(i, j)}{\partial x} \sin \theta + \frac{\partial p(i, j)}{\partial y} \cos \theta, \quad (8)$$

where $\theta = 77^\circ$ is wire pitch angle (see Fig. 6a).

3. Measurement campaigns

The measurement campaign consists of six flow rate values whose corresponding Reynolds numbers are calculated based on the bundle's hydraulic diameter $D_h = 4A/P_h$, where A is the bundle flow area, and P_h is the corresponding wetted perimeter, following (Todreas and Kazimi, 1990). Table 2 reports the water temperature of the experiments and the corresponding Reynolds number for the several investigated flow rates.

The PIV measurements consist of 10,000 images collected at a rate of 18 frames per second. The location of the measurement region is shown in Fig. 2. The laser sheet enters the outer hexagonal Perspex casing (Fig. 2a) and it goes through the FEP, reaching the central wire spacer where the measurement region is located (red rectangle in Fig. 2b). For a preliminary measurement, the laser sheet is moved closer to the rod (Fig. 2b, dashed profile in view B-B) in order to study the flow area downstream the wire. The second, and main, measurement campaign is conducted with the laser sheet closer to the bulk region of the subchannel, being tangent to the central rod's wire spacer. The flow area in front of the helicoid spacer is thus investigated.

3.1. Time-averaged velocity fields

A preliminary measurement campaign has studied the fluid region downstream the wire (see Fig. 2b, view B-B), showing that the flow follows the helical path of the wire, as expected, contributing to the mixing. This is evident in Fig. 3a where the blue colour indicates a negative direction of the u component (towards the left). Fig. 3b, however, shows that if the measurement region is moved at the front of the wire, closer to the bulk of the subchannel, the fluid changes direction moving against the wire's path. This is clear from the red colour that shows a positive u , hence a flow in the positive x direction. The two measurement areas are approximately 2 mm apart in the out-of-plane direction. The area shown in Fig. 2a is locally aligned with the wire. In order to illuminate the region downstream of the wire, the laser is blocked by the metal surface of the wire and thus it does not reach the

region to the left in the figure. This flow behaviour, called "migratory flow" in Ohtake et al. (1976), was ascribed to the increased hydraulic resistance that the wire causes in the subchannel.

The velocity fields shown hereafter focus on the flow in front of the central wire where the migratory flow is observed. The measured quantities are the stream-wise and span-wise velocity components v and u , respectively. These are normalised by the bulk velocity, which is defined as $V_b = Q/A$, being Q the volumetric flow rate, and A the total bundle's flow area. In small rod bundles such as the one of this work, dimensional tolerances of the components (rods, wires, Perspex outer case) play an important role. A deviation in the thickness of the outer hexagonal wall from the nominal value could affect the flow area in the cross section, thereby affecting the estimation of the bulk velocity. For example, it has been estimated that a deviation of 1 mm in the wall thickness could change the bulk velocity by as much as 18%.

Fig. 4 shows the contour plot of the time-averaged axial velocity component v , for the considered values of Reynolds numbers. A low-speed region appears at the downstream side of the wire, which is also found in Goth et al. (2018). This low-speed region is more spread-out at the lower Reynolds numbers and it becomes narrower as the Reynolds increases.

Fig. 5 shows the contour plot of the normalised time-averaged span-wise velocity component u for the six studied Reynolds numbers. The positive sign of the lateral velocity component means that the flow coming from the top bends towards the right as it approaches the wire, as shown in Fig. 6b. The figure shows that the relative magnitude of u is slightly higher at lower Reynolds numbers, meaning that the flow tends to bend more markedly at lower flow rates. The next section will provide a description of the bending angle of the flow.

4. Modelling of migratory flow

The time-averaged velocity fields reported in Fig. 4 and 5 show that the flow near the wire bends against the wrapping direction of the helicoid spacer (as modelled in Fig. 6a), if the flow is measured at the front of the wire. This section discusses the theory through which this behaviour is modelled and explained.

4.1. Euler equations in the streamline's coordinate system

This section makes use of the Euler equation in the streamline's coordinate system to provide an equation that models the pressure gradient normal to the wire. The steady state Navier–Stokes equation where the viscous term is neglected is known as Euler equation:

Table 2
Experimental conditions of the experiments.

Q [m ³ s ⁻¹]	T [°C]	Re
9.00×10^{-4}	32.4	4990
1.37×10^{-3}	32.3	7580
1.80×10^{-3}	32.2	9940
2.30×10^{-3}	32.0	12650
2.70×10^{-3}	31.7	14760
2.95×10^{-3}	32.3	16330

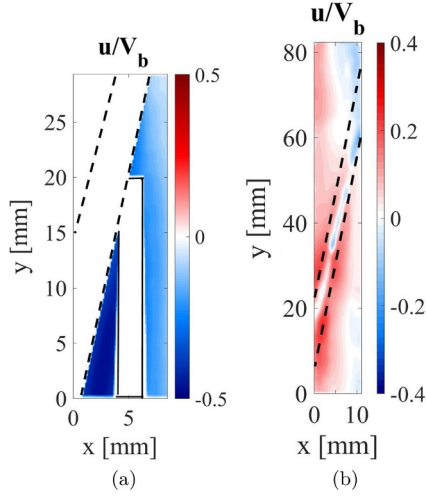


Fig. 3. a) Contour plot of the lateral component u measured beneath the wire; the dashed line indicates the wire's position, whereas the solid line bounds the masked-out area affected by reflection. b) Contour plot of the u component measured at the front of the wire, closer to the bulk; the dashed line marks the borders of the wire. The main flow is from top to bottom.

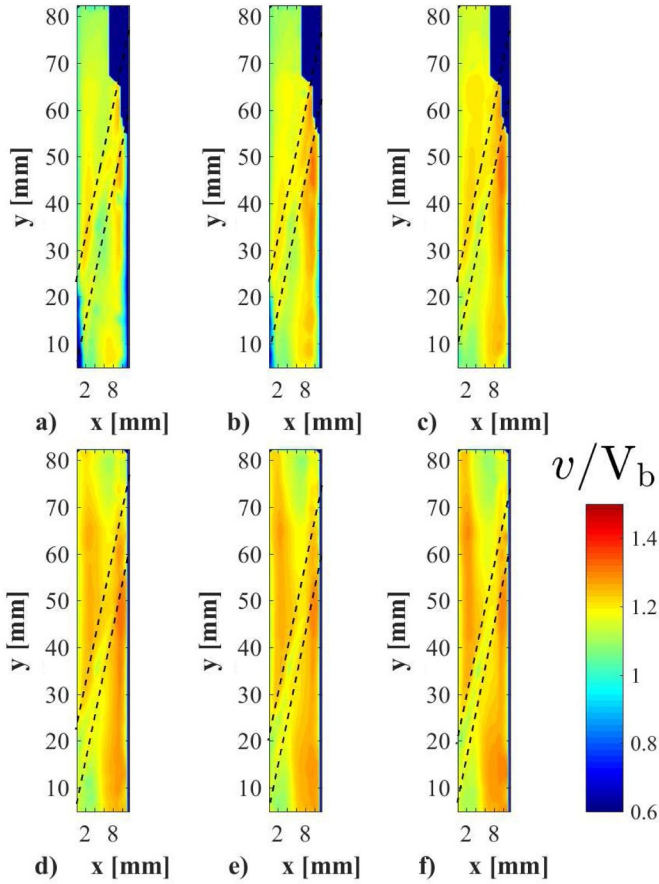


Fig. 4. Stream-wise time-averaged velocity component v normalised to the bulk velocity V_b . a) $Re = 4990$; b) $Re = 7580$; c) $Re = 9940$; d) $Re = 12650$; e) $Re = 14760$; f) $Re = 16330$. The main flow is from top to bottom. The cases a, b, and c have the upper-right corner masked-out due to reflections.

$$(\vec{U} \cdot \nabla) \vec{U} = -\nabla p + \rho \mathbf{g}, \quad (9)$$

where \vec{U} is the velocity vector. Fig. 6a sketches a streamline that bends as the fluid approaches the wire spacer. The main flow is in the negative y direction in the figure. A sample of the real time-averaged streamline

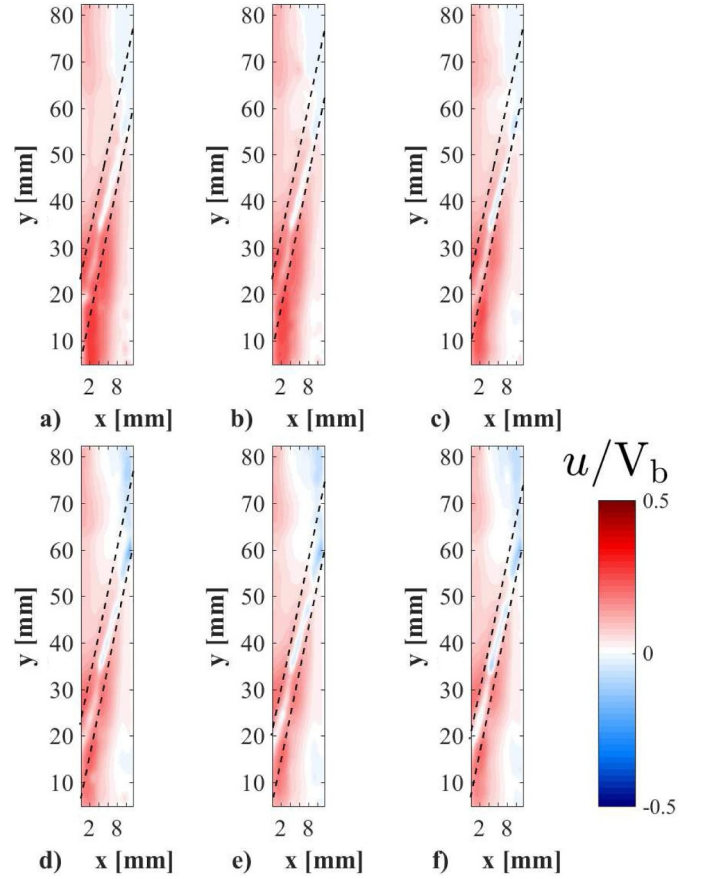


Fig. 5. Span-wise velocity component u normalised to the bulk velocity V_b , overlapped to the vectorial field. a) $Re = 4990$; b) $Re = 7580$; c) $Re = 9940$; d) $Re = 12650$; e) $Re = 14760$; f) $Re = 16330$. The main flow is from top to bottom.

distribution is shown in Fig. 6b. The streamlines are superimposed to the field of the lateral (span-wise) velocity component. It is convenient to express the Euler equations in the streamline's reference frame, being \hat{e}_s and \hat{e}_n the unit vectors tangential and normal to the streamline, respectively. The velocity vector $U\hat{e}_s$ is, by definition, always tangent to the streamline, and the gradient operator is defined as $\nabla \equiv \frac{\partial}{\partial s}\hat{e}_s + \frac{\partial}{\partial n}\hat{e}_n$. By doing so, Eq. 9 takes the form reported in Fox et al. (2011)

$$U^2 \frac{\partial \hat{e}_s}{\partial s} + U \frac{\partial U}{\partial s} \hat{e}_s = -\frac{1}{\rho} \left(\frac{\partial p}{\partial s} \hat{e}_s + \frac{\partial p}{\partial n} \hat{e}_n \right) + \mathbf{g} \left(\frac{\partial y}{\partial s} \hat{e}_s + \frac{\partial y}{\partial n} \hat{e}_n \right), \quad (10)$$

where

$$\frac{\partial \hat{e}_s}{\partial s} = -\frac{1}{R} \hat{e}_n; \quad \frac{\partial y}{\partial s} = \cos \beta; \quad \frac{\partial y}{\partial n} = \sin \beta, \quad (11)$$

being R the local curvature radius of the streamline and β the angle that the streamline forms with the vertical (see Fig. 6a for reference). R is calculated as in Zorich (2004)

$$R = \left[1 + \left(\frac{dx}{dy} \right)^2 \right]^{3/2} \left(\frac{d^2x}{dy^2} \right)^{-1}, \quad (12)$$

where dx/dy is the derivative of the streamline along the stream-wise direction y . The component of Eq. 10 normal to the streamline (along \hat{e}_n) becomes then

$$-\frac{U^2}{R} = -\frac{1}{\rho} \frac{\partial p}{\partial n} + g \sin \beta. \quad (13)$$

This equation is responsible for the bending of the streamlines, meaning that when gravity is not considered, the pressure decreases towards the centre of curvature of the streamline (Fay, 1994). The

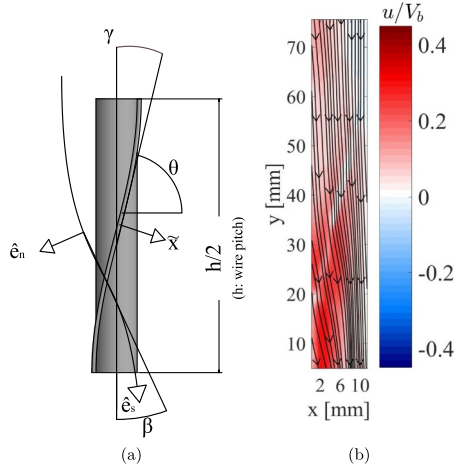


Fig. 6. a) Deflection of a streamline near the wire spacer; the Euler equations are applied in the streamline's frame of reference \hat{e}_n, \hat{e}_s to reconstruct the pressure gradient field normal to the wire. \bar{x} is the direction normal to the wire. b) Example of the mean velocity's streamlines superimposed to the lateral velocity component.

component of Eq. 10 parallel to the streamline (along \hat{e}_s) gives the well-known Bernoulli equation, where the term $\partial p/\partial s$ is responsible for the acceleration of the fluid along the streamline:

$$U \frac{\partial U}{\partial s} = -\frac{1}{\rho} \frac{\partial p}{\partial s} + g \cos \beta. \quad (14)$$

From Eqs. 13 and 14 it follows that the components of the pressure gradient are

$$\frac{\partial p}{\partial n} = \rho \left(\frac{U^2}{R} + g \sin \beta \right), \quad \frac{\partial p}{\partial s} = -\rho \left(U \frac{\partial U}{\partial s} + g \cos \beta \right), \quad (15)$$

where the derivative of the velocity along a streamline, $\partial U/\partial s$, is computed as

$$\frac{\partial U}{\partial s} = \frac{U_{i+1} - U_{i-1}}{s_{i+1} - s_{i-1}}, \quad (16)$$

with the indices $i + 1$ and $i - 1$ referring to the points along the streamline. The pressure gradient normal to the wire (\bar{x} direction) is evaluated as

$$\frac{\partial p}{\partial \bar{x}} = \frac{\partial p}{\partial n} \sin(\theta - \beta) + \frac{\partial p}{\partial s} \cos(\theta - \beta), \quad (17)$$

where $\theta = 77^\circ$ is the wire's pitch angle (see Fig. 6a). This equation can be used to estimate the pressure gradient normal to the wire as a tool to explain the experimental results regarding the flow direction.

4.2. An equation for the bending of the streamlines

This section aims at deriving an equation that describes and quantifies the bending of the flow streamline due to the proximity of the wire spacer. By doing so, our understanding of the physics at play improves. We start from the Euler equation across a streamline (Eq. 13) that, without gravitational effects, is

$$-\frac{U^2(\vec{r})}{R(\vec{r})} \hat{e}_n = -\frac{1}{\rho} \frac{\partial p(\vec{r})}{\partial n} \hat{e}_n, \quad (18)$$

where $\vec{r} = (x, y)$ is the position in the two-dimensional flow field.

A streamline is defined as the locus of points always tangent to the local velocity, as explained in Tropea et al. (2007):

$$\frac{dx}{dy} = \frac{u(\vec{r})}{v(\vec{r})} \quad (19)$$

where $u(\vec{r})$ and $v(\vec{r})$ are the velocity components along any streamline. For any particular streamline $s = (\psi(y), y)$ it follows that

$$\frac{d\psi(y)}{dy} = \frac{u(\vec{r})}{v(\vec{r})} = \frac{U \sin \beta(\vec{r})}{U \cos \beta(\vec{r})} = \tan \beta(\vec{r}), \quad (20)$$

which is expressed in terms of the angle β that the streamline forms with the vertical (see Fig. 6a). The velocity magnitude U is then expressed as

$$U^2(\vec{r}) = v^2(\vec{r}) [1 + \tan^2 \beta(\vec{r})]. \quad (21)$$

Upon substitution of Eq. 21, Eq. 18 becomes

$$\rho \frac{v^2(\vec{r})}{R(\vec{r})} [1 + \tan^2 \beta(\vec{r})] \hat{e}_n = \frac{\partial p(\vec{r})}{\partial n} \hat{e}_n. \quad (22)$$

Considering a single streamline ($\psi(y), y$) and recalling the definition of R (Eq. 12), the previous equation becomes

$$\rho v^2(\vec{r}) [1 + \tan^2 \beta(\vec{r})] \frac{d^2 \psi(y)}{dy^2} \left[1 + \left(\frac{d\psi(y)}{dy} \right)^2 \right]^{-3/2} \hat{e}_n = \frac{\partial p(\vec{r})}{\partial n} \hat{e}_n. \quad (23)$$

From Eq. 20 $\tan \beta(\vec{r})$ replaces the $d\psi(y)/dy$ term, hence

$$\begin{aligned} \rho v^2(\vec{r}) \frac{1 + \tan^2 \beta(\vec{r})}{[1 + \tan^2 \beta(\vec{r})]^{3/2}} \frac{d^2 \psi(y)}{dy^2} \hat{e}_n &= \frac{\rho v^2(\vec{r})}{[1 + \tan^2 \beta(\vec{r})]^{1/2}} \frac{d^2 \psi(y)}{dy^2} \hat{e}_n \\ &= \frac{\partial p(\vec{r})}{\partial n} \hat{e}_n. \end{aligned} \quad (24)$$

The second order derivative term is rearranged as

$$\frac{d^2 \psi(y)}{dy^2} = [1 + \tan^2 \beta(\vec{r})] \frac{d\beta(\vec{r})}{dy}, \quad (25)$$

and substituted into Eq. 24, to obtain an expression relating the pressure gradient normal to the streamline with the local angle of inflection $\beta(\vec{r})$:

$$\frac{1}{\rho v^2(\vec{r})} \frac{\partial p(\vec{r})}{\partial n} = [1 + \tan^2 \beta(\vec{r})]^{1/2} \frac{d\beta(\vec{r})}{dy}. \quad (26)$$

In order to obtain $\beta(\vec{r})$, Eq. 26 is integrated in dy on both sides along the considered streamline $s = (\psi(y), y)$. The integral is estimated between $y = -\infty$, far upstream, where the influence of the wire is negligible and the streamline is straight ($\beta = 0$), and the generic coordinate $y = \sigma$ along the streamline. By moving all the terms that do not contain $\beta(\vec{r})$ to the right-hand side of the equation, we get

$$\int_{-\infty}^{\sigma} [1 + \tan^2 \beta(\vec{r})]^{1/2} \frac{d\beta(\vec{r})}{dy} dy = \int_{-\infty}^{\sigma} \frac{1}{\rho v^2(\vec{r})} \frac{\partial p(\vec{r})}{\partial n} dy. \quad (27)$$

Assuming that the streamline far upstream of the wire is straight, i.e. $\beta(y = -\infty) = 0$, the left-hand side term becomes

$$\int_0^{\beta(y=\sigma)} [1 + \tan^2 \beta(\vec{r})]^{1/2} d\beta(\vec{r}) = \int_{-\infty}^{\sigma} \frac{1}{\rho v^2(\vec{r})} \frac{\partial p(\vec{r})}{\partial n} dy. \quad (28)$$

Considering that

$$1 + \tan^2 \beta(\vec{r}) = \frac{1}{\cos^2 \beta(\vec{r})}, \quad (29)$$

it follows that

$$\int_0^{\beta(y=\sigma)} \frac{1}{\cos \beta(\vec{r})} d\beta(\vec{r}) = \int_{-\infty}^{\sigma} \frac{1}{\rho v^2(\vec{r})} \frac{\partial p(\vec{r})}{\partial n} dy. \quad (30)$$

Solving the integral at the left hand side of the previous equation leads to

$$\frac{1}{2}[\ln(1 + \sin \beta(y = \sigma)) - \ln(1 - \sin \beta(y = \sigma))] = \int_{-\infty}^{\sigma} \frac{1}{\rho v^2(\vec{r})} \frac{\partial p(\vec{r})}{\partial n} dy, \quad (31)$$

where the Taylor expansion is applied to the logarithm. For small $\beta(\vec{r})$,

$$\sin \beta(\vec{r}) \approx \beta(\vec{r}), \quad (32)$$

so

$$\beta(y = \sigma) = \int_{-\infty}^{\sigma} \frac{1}{\rho v^2(\vec{r})} \frac{\partial p(\vec{r})}{\partial n} dy. \quad (33)$$

Using Eq. 11, the previous equation can be rewritten as

$$\beta(y = \sigma) = \int_{-\infty}^{\sigma} \frac{1}{\rho v^2(\vec{r})} \frac{\partial p(\vec{r})}{\partial n} \cos \beta(\vec{r}) ds. \quad (34)$$

For small β , the cosine can, thus, be neglected. Such an approximation leads to

$$\beta(y = \sigma) = \int_{-\infty}^{\sigma} \frac{1}{\rho v^2(\vec{r})} \frac{\partial p(\vec{r})}{\partial n} ds. \quad (35)$$

This final equation gives the value of β as the result of a path integral over a streamline. It is clear from Eq. 35 that the bending of flow is determined by the interplay of the transverse pressure gradient and inertia. Furthermore, it is interesting to observe that the value of the bending angle at a certain coordinate s along a streamline depends on the upstream path, as indicated by the need of solving the integral. Approximating the left hand side of Eq. 31 assuming that β is small is accurate within an error of 5% for $\beta \in [0, \pi/3]$, and within 12% for $\beta \in [0, \pi/4]$. This values are obtained by comparing the left hand side term of Eq. 31 with β itself over the interval $[0, \pi/2]$.

5. Results

In the first part of this section, the results of the model based on the Euler equations are shown; they consist of the pressure gradient fields evaluated normal to the wire. These are then compared to the experimental results, being the pressure gradient field derived from the 2D Navier–Stokes equations. Finally, Eq. 35, which predicts the bending angle β , is compared to the experimental results.

5.1. Pressure gradient normal to the wire predicted by the Euler equations

This section presents the reconstructed pressure gradient modelled through the Euler equation, following the approach discussed in section 4. Eq. 17 is applied to the streamlines to estimate the local, non-dimensional pressure gradient normal to the wire, $\frac{2D_w}{\rho V_b^2} \frac{\partial p}{\partial \tilde{x}}$, where $1/2\rho V_b^2$ is the dynamic pressure, and D_w the wire diameter. Fig. 7 shows the pressure gradient field normal to the wire, along the \tilde{x} direction (see Fig. 6a for the reference system).

Fig. 7 shows that the negative pressure gradient bends the streamlines towards the wire, leading to the lateral velocity field previously shown in Fig. 5. Thereafter, the flow enters the downstream region, where the pressure increases with \tilde{x} (positive $\partial p/\partial \tilde{x}$) throughout the recirculation region, similarly to the experiments reported in Biswas et al. (2004) with a backward-facing step. Here the positive pressure gradient tends to straighten the streamline, decreasing thus the bending angle. The flow region over the wire is not shown due to reflection of light from the metal surface of the wire that does not allow the PIV software to keep track of the particle positions in the fluid.

5.2. –Comparison with the pressure gradient predicted by the Navier-Stokes equation

The pressure gradient normal to the wire estimated by the model

based on the Euler equations is compared with the solution given by the Navier–Stokes equation (Section 2.3, Eq. 8). Fig. 7 shows the pressure gradient field predicted by the Euler equations; Fig. 8 shows the pressure gradient field obtained from solving the two-dimensional Navier–Stokes equations. The pressure gradient normal to the wire based on the Euler equations is confirmed by the results of the Navier–Stokes equations, where the viscous effects are taken into account and the only assumption is that the flow is two-dimensional. Since the model predicts the pressure gradient in the fluid along the perpendicular direction to the wire, a reference line also orthogonal to it is chosen to perform a quantitative comparison. The line is shown in Fig. 8f, for the six investigated Reynolds numbers. The results of such a comparison are plotted in Fig. 9.

Fig. 9 shows the plot of $\frac{\partial p}{\partial \tilde{x}}$ modelled by applying the Euler equation to the flow streamlines (○) and calculated from the Navier–Stokes equations (□). The abscissa \tilde{x} is the coordinate over the line normal to the wire chosen for the comparison (Fig. 8f). The error bars associated with the model (black circles) are based on the error resulting from fitting the velocity field with the streamlines. The error bars associated with the results of the Navier–Stokes equations applied to the measured velocity fields (blue squares) are based on statistical deviation around the mean value. The figure shows good agreement between the two data series. Firstly, this proves that the model based on the Euler equations is consistent, and secondly that the viscous effects (neglected in the model) do not play a significant role in such a flow.

5.3. Validating the predicted bending angle against the experiments

In this section the bending angle β , predicted by Eq. 35, is compared

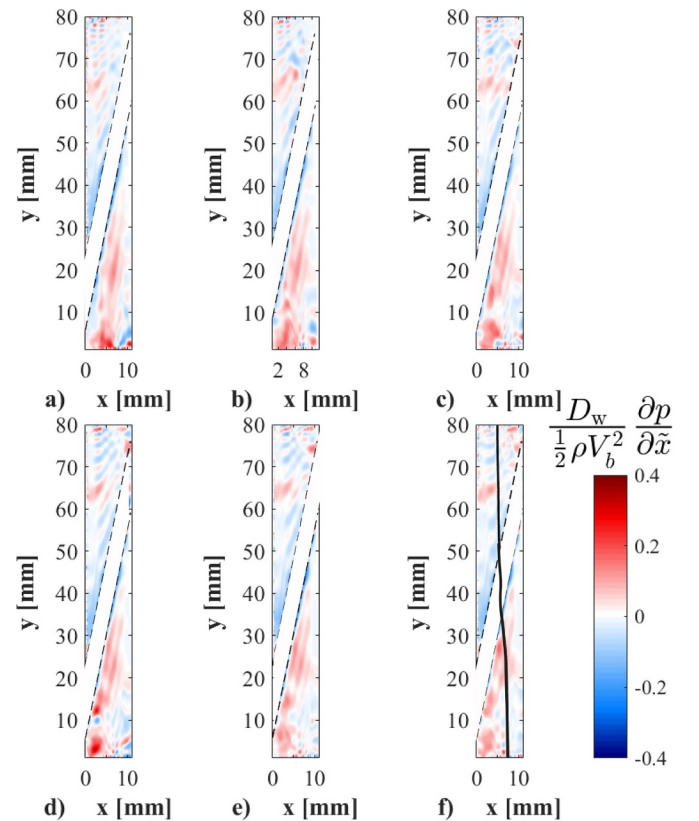


Fig. 7. Mean non-dimensional pressure gradient normal to the wire spacer modelled through the Euler equations. The flow is from top to bottom; a) $Re = 4990$; b) $Re = 7580$; c) $Re = 9940$; d) $Re = 12650$; e) $Re = 14760$; f) $Re = 16330$; an exemplifying streamline is also reported. The flow region over the wire is not shown due to reflection of light.

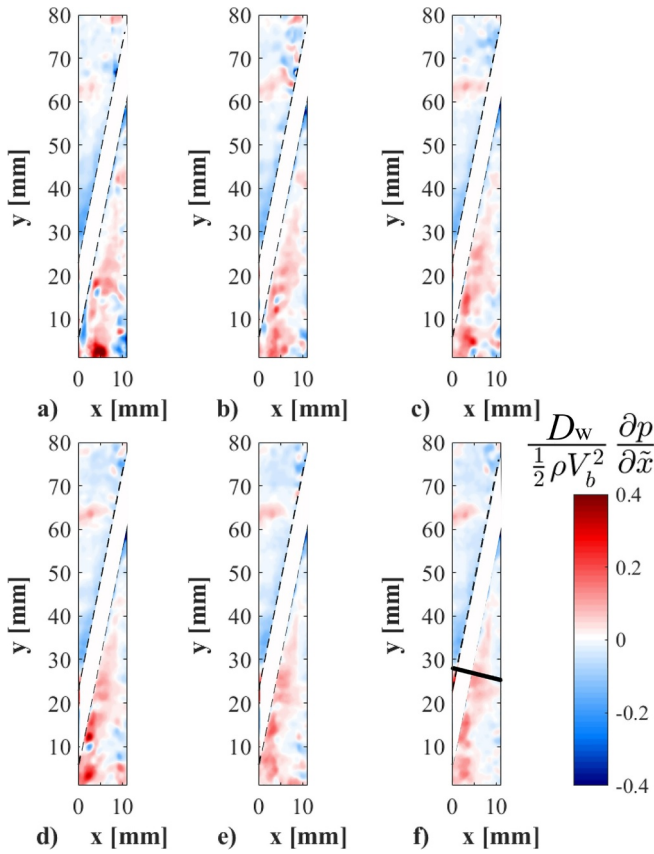


Fig. 8. Time-averaged non-dimensional pressure gradient normal to the wire, computed from the two-dimensional Navier–Stokes equations. The flow is from top to bottom. a) $Re = 4990$; b) $Re = 7580$; c) $Re = 9940$; d) $Re = 12650$; e) $Re = 14760$; f) $Re = 16330$; the black line is followed for extracting the numerical values for comparison. The flow region over the wire is not shown due to reflection of light.

with the angle obtained from the time-averaged velocity fields measured with PIV. Based on the PIV measurements, β along the streamline is evaluated following Eq. 20 as

$$\beta(\vec{r}) = \arctan \left[\frac{u(\vec{r})}{v(\vec{r})} \right]. \quad (36)$$

The results are plotted in Fig. 10 against the normalised coordinate s along the considered streamline. The error bars are based on the statistical deviation of the measured velocity components. The accuracy on the prediction of β is expressed as the normalised root mean square error (NRMSE):

$$\text{NRMSE} = \frac{\sqrt{\frac{1}{N_s} \sum_{i=1}^{N_s} ([\beta(i)]_{\text{Eq.35}} - [\beta(i)]_{\text{PIV}})^2}}{(\beta_{\text{max}})_{\text{PIV}} - (\beta_{\text{min}})_{\text{PIV}}}, \quad (37)$$

where N_s is the number of points along the streamline where the pressure gradient is evaluated, and the subscript PIV refers to the angle retrieved from the measured velocity fields. The error thus evaluated is 8%: most of the contribution to the error is located in the measured region closest to the wire, being $s(y)/L = 0.47 - 0.55$, where reflections of light coming from the metal wire may affect the measurement. The new expression derived for estimating β proves to be a valid alternative to the Euler equations for linking the pressure gradient to the corresponding bending angle β , being the latter more easily measurable than the curvature radius. The bending angle measured at one location (on the edge of the wire) is not a function of the Reynolds number, being constant for all the investigated flow rates. This is shown in Fig. 11. Since β is related to the velocity components by $\tan \beta = u/v$ (see Eq. 20), a constant bending angle means that the ratio between the flow

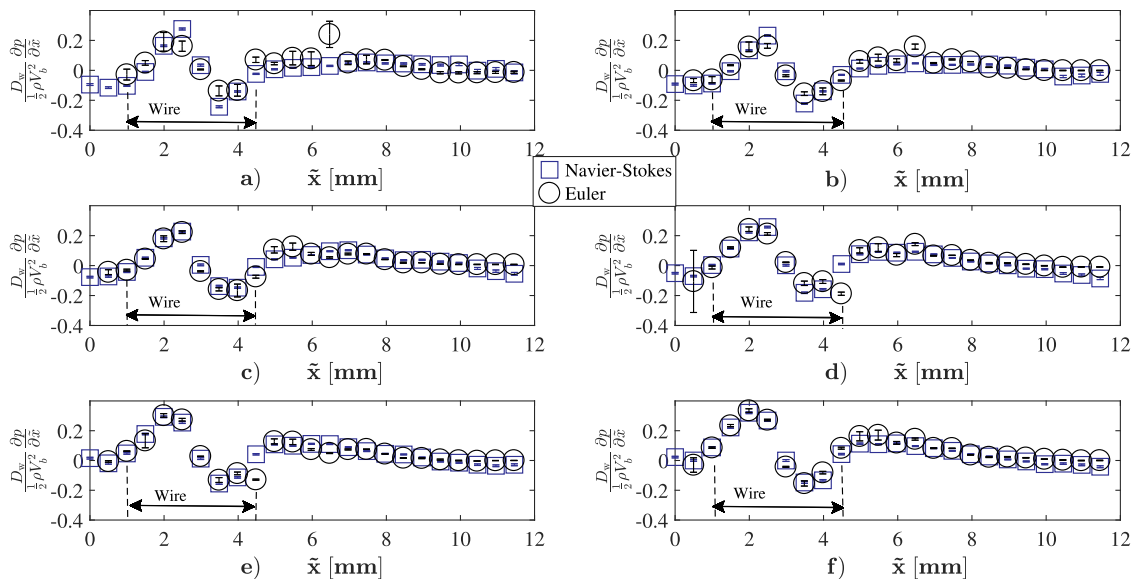


Fig. 9. Non-dimensional pressure gradient normal to the wire predicted by the Euler equations (○, Eq. 17) compared to the results obtained with the Navier–Stokes equations (□, Eq. 8). a) $Re = 4990$; b) $Re = 7580$; c) $Re = 9940$; d) $Re = 12650$; e) $Re = 14760$; f) $Re = 16330$.

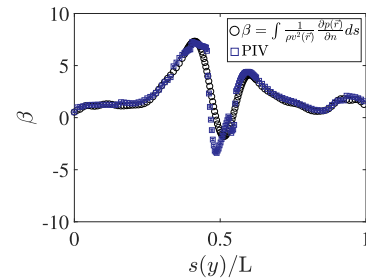


Fig. 10. Bending angle β along a streamline evaluated with Eq. 35 derived in Section 4.2 (○) compared with the angle obtained from the PIV measurements (□). The abscissa is normalised by the streamline's total length. $Re = 16330$.

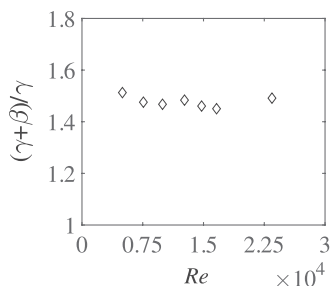


Fig. 11. Measured bending angle of the flow streamline for different Reynolds numbers. γ is the wire pitch angle equal to 13° .

components remains constant as well. This might explain how the pressure gradient fields (which determine the angle of bending) appear to be independent on the Reynolds number (Fig. 7), even if the velocity component fields are not (Fig. 4, 5).

6. Conclusions

This work aimed at investigating, modelling, and thereby explaining the migratory flow close to the helicoid wire spacer inside a 7-rods, wire-wrapped hexagonal bundle by reconstructing the pressure gradient in the direction normal to the wire. Experiments have been performed inside the rod bundle, where the axial flow has been investigated with Particle Image Velocimetry, making use of a refractive index-matching technique to reduce refraction of light inside the test section. Six Reynolds numbers were considered, at which the time-averaged velocity fields were measured. The results show that the flow downstream the wire followed the helicoid path, as expected. However, if the investigated region was moved to the front of the wire, closer to the bulk of the subchannel, the flow changed the direction by moving against the wire's helicoid path. The pressure gradient normal to the wire has been modelled through the Euler equations applied to the streamlines, thereby showing that the bending of the flow is caused by the pressure gradient imposed by the wire. The results modelled through the Euler equations were compared with the solution of the two-dimensional Navier–Stokes equations leading to a good qualitative and quantitative agreement. Furthermore, an expression to predict the bending angle of the flow has been derived and successfully validated against the experimental results. The findings of this work give more insight into the physics governing the bending of the flow close to the wire spacer, highlighting how the flow bending is determined by the interplay of the transverse pressure gradient and inertia of the flow. Nevertheless, the model hereby presented leads the way to future possibilities for evaluating the bending angle through macroscopic, known variables such as bundle dimensions and flow rate.

Acknowledgements

This project has received funding from the Euratom research and training programme 2014–2018 under the grant agreement No. 654935.

The author would like to thank Ing. Dick de Haas and Ing. John Vlieland for the technical support provided during the work.

References

Bertocchi, F., Rohde, M., Kloosterman, J.L., 2018. LDA measurements of coherent flow structures and cross-flow across the gap of a compound channel with two half-rods. *Nuclear Eng. Des.* 326, 17–30. <https://doi.org/10.1016/j.nucengdes.2017.10.023>.

Biswas, G., Breuer, M., Durst, F., 2004. Backward-facing step flows for various expansion ratios at low and moderate Reynolds numbers. *J. Fluids Eng.* 126, 362–374. <https://doi.org/10.1115/1.1760532>.

Brockmeyer, L., Carasik, L.B., Merzari, E., Hassan, Y., 2017. Numerical simulations for determination of minimum representative bundle size in wire wrapped tube bundles. *Nuclear Eng. Des.* 322, 577–590. <https://doi.org/10.1016/j.nucengdes.2017.06.038>.

De Ridder, J., Degroote, J., Vierendeels, J., Van Tichelen, K., 2016. Vortex-induced vibrations by axial flow in a bundle of cylinders. *Proc. 11th International Conference on Flow-Induced Vibrations, The Hague, The Netherlands*. pp. 1–8.

Dominguez-Ontiveros, E.E., Hassan, Y.A., 2009. Non-intrusive experimental investigation of flow behavior inside a 5×5 rod bundle with spacer grids using PIV and MIR. *Nuclear Eng. Des.* 239, 888–898. <https://doi.org/10.1016/j.nucengdes.2009.01.009>.

Fay, J.A., 1994. *Introduction to Fluid Mechanics*. MIT Press.

Fischer, P., Lottes, J., Siegel, A., 2007. Large Eddy Simulation of wire-wrapped fuel pins I: hydrodynamics of a single pin. *Proc. Joint Int. Topical Meeting on Mathematics & Computation and Supercomputing in Nuclear Applications (M&C + SNA 2007)*, Monterey, CA USA.

Fox, R.W., McDonald, A.T., Pritchard, P., Leylegian, J.C., 2011. *Fox and McDonald's Introduction to Fluid Mechanics*. Wiley.

Goth, N., Jones, P., Nguyen, D.T., Vaghetto, R., Hassan, Y., Obabko, A., Merzari, E., Fischer, P.F., 2018. Comparison of experimental and simulation results on interior subchannels of a 61-pin wire-wrapped hexagonal fuel bundle. *Nuclear Eng. Des.* 338 (August), 130–136. <https://doi.org/10.1016/j.nucengdes.2018.08.002>.

Hosokawa, S., Yamamoto, T., Okajima, J., Tomiyama, A., 2012. Measurements of turbulent flows in a 2×2 rod bundle. *Nuclear Eng. Des.* 249, 2–13. <https://doi.org/10.1016/j.nucengdes.2011.11.035>.

Idel'chik, I.E., 1966. *Handbook of hydraulic resistance*. Israel Program for Scientific Translations.

de Kat, R., van Oudheusden, B.W., 2010. Instantaneous planar pressure from PIV: analytic and experimental test-cases. *Proc. 15th Int. Symposium on Applications of Laser Techniques to Fluid Mechanics, Lisbon, Portugal, July*.

de Kat, R., van Oudheusden, B.W., 2011. Instantaneous planar pressure determination from PIV in turbulent flow. *Exp. Fluids* 52, 1089–1106. <https://doi.org/10.1007/s0034801112375>.

Mahmood, A., 2011. *Single-phase crossflow mixing in a vertical tube bundle geometry - an experimental study*. Delft University of Technology Ph.D. thesis.

Merzari, E., Fischer, P., Yuan, H., Tichelen, K.V., Keijers, S., Ridder, J.D., Degroote, J., Vierendeels, J., Doolaard, H., Gopala, V.R., Roelofs, F., 2016. Benchmark exercise for fluid flow simulations in a liquid metal fast reactor fuel assembly. *Nuclear Eng. Des.* 298, 218–228. <https://doi.org/10.1016/j.nucengdes.2015.11.002>.

Moorthi, A., Sharma, A.K., Velusamy, K., 2018. A review of sub-channel thermal hydraulic codes for nuclear reactor core and future directions. *Nuclear Eng. Des.* 332, 329–344. <https://doi.org/10.1016/j.nucengdes.2018.03.012>.

Nguyen, T., Goth, N., Jones, P., Lee, S., Vaghetto, R., Hassan, Y., 2017. PIV measurements of turbulent flows in a 61-pin wire-wrapped hexagonal fuel bundle. *Int. J. Heat Fluid Flow* 65, 47–59. <https://doi.org/10.1016/j.ijheatfluidflow.2017.03.007>.

Nguyen, T., Goth, P., Jones, P., Vaghetto, R., Hassan, Y., 2018. Stereoscopic PIV measurements of near-wall flow in a tightly packed rod bundle with wire spacers. *Int. J. Heat Fluid Flow* 92, 420–435. <https://doi.org/10.1016/j.expthermflusci.2017.11.009>.

Nguyen, T., Hassan, Y., 2017. Stereoscopic particle image velocimetry measurements of flow in a rod bundle with a spacer grid and mixing vanes at a low Reynolds number. *Int. J. Heat Fluid Flow* 67, 202–219. <https://doi.org/10.1016/j.ijheatfluidflow.2017.08.011>.

Obabko, A.V., Merzari, E., Fischer, P.F., 2016. Nek5000 large eddy simulations for thermal-hydraulics of deformed wire-wrap fuel assemblies. *Transactions of the American Nuclear Society (ANS 2016)*, Las Vegas, USA.

Ohtake, T., Uruwashi, S., Takahashi, K., 1976. Velocity measurements in the subchannel of the wire-spaced subassembly. *Nuclear Technol.* 30, 333–349. <https://doi.org/10.13182/NT76-A31648>.

Pointer, W.D., Fischer, P., Siegel, A., 2008. RANS-based CFD Simulations of Wire-Wrapped Fast Reactor Fuel Assemblies. *Proc. ICAPP '08, Anaheim, CA USA*.

Sato, H., Kobayashi, J., Miyakoshi, H., Kamide, H., 2009. Study on velocity field in a wire wrapped fuel pin bundle of sodium cooled reactor - Detailed Velocity Distribution in a Subchannel -. *Proc. 13th Int. Topical Meeting on Nuclear Reactor Thermal Hydraulics (NURETH-13)*, Kanazawa, Japan.

Shams, A., Roelofs, F., Baglietto, E., Komen, E.M.J., 2018. High fidelity numerical simulations of an in finite wire-wrapped fuel assembly. *Nuclear Eng. Des.* 335, 441–459. <https://doi.org/10.1016/j.nucengdes.2018.06.012>.

Song, M.S., Jeong, J.H., Kim, E.S., 2019. Numerical investigation on vortex behavior in wire-wrapped fuel assembly for a sodium fast reactor. *Nuclear Eng. Des.* 51, 665–675. <https://doi.org/10.1016/j.net.2018.12.012>.

Todreas, N.E., Kazimi, M.S., 1990. *Nuclear Systems I: Thermal Hydraulic Fundamentals*. Vol. 1. Taylor & Francis.

Tropea, C., Yarin, A.L., Foss, J.L., 2007. *Springer Handbook of Experimental Fluid Mechanics*. Springer.

Westerweel, J., 1994. Efficient detection of spurious vectors in particle image velocimetry data. *Exp. Fluids* 247, 236–247. <https://doi.org/10.1007/BF00206543>.

Zorich, V.A., 2004. *Mathematical Analysis I*. Springer.